Studienarbeit

Particle Image Velocimetry measurements on a birdlike airfoil

Alba Pascual Massana
Matr.Nr. 2957551

Tutor: Dipl.-Ing. Stephan Bansmer

Institut of Fluid Mechanics
Prof. Dr.-Ing. Rolf Radespiel
Technische Universität Braunschweig

September 2008

INDEX

1 INTRODUCTION

The objective of this project is to study the aerodynamics around a birdlike airfoil. The variables to investigate are the turbulent shear stress and the pressure distribution. With this aim, two experiments were carried out in the LNB wind tunnel.

The seagull hand pinion inspired the SG04 birdlike airfoil considered for this work. A flapping flight motion apparatus was used to force this wing heaving and pitching.

First, an experiment to capture the boundary layer and determine the shear stress was done. Therefore, very accurate measurements with stereoscopic Particle Image Velocimetry technique were required. This exercise was performed with a flexible and non-flexible SG04 wing.

Moreover, with the same method, a second experiment tried to capture a larger flow field around the whole flexible flapping SG04 airfoil, in order to determine the pressure distribution.

To begin with, a theoretical background highlighting the most important features of moving airfoils and Particle Image Velocimetry is presented. The experimental setup, recording, data processing and results of both experiments conclude the second part of this work.

2 THEORETICAL BACKGROUND

Before entering in detail into the experiments, an overview on the two most important topics of this work is to be done in this chapter: moving airfoils and Particle Image Velocimetry technique.

2.1 Moving airfoils

The flapping airfoil focus of study in here comprises two movements: heaving $-z(t)-$ and pitching $-\alpha(t)-$ (see Fig.2-1) [1]. Their two-degree-of-fredoom movement is depicted by the following pair of equations:

$$z(t) = \hat{z} \cdot \cos(wt)$$

$$\alpha(t) = \hat{\alpha} \cdot \cos(wt + \pi/2) + \alpha_0$$

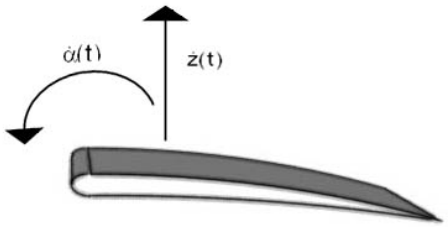

Fig. 2-1 Flapping airfoil

Since this airfoil flaps up and down, its geometrical angle of attack is altered with the approaching flow (see Fig.2-2). This variation $-\zeta(t)-$ depends on the flow and heaving velocity, as showed in the next equation: $\zeta(t) = \text{arctg}(-\dot{z}(t)/U_\infty)$.

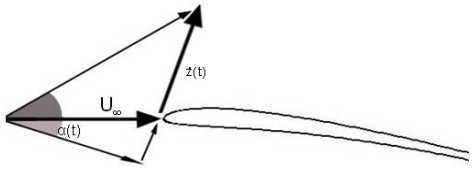

Fig. 2-2 Geometrical angle of attack and its variation constitute the effective angle of attack

The effective angle of attack is the sum of the geometrical angle and the variation:

$$\alpha_{eff}(t) = \alpha(t) + \zeta(t) .$$

▪ Specific case

In the flapping part experiments (see chapter 3 and 4), the airfoil's angle was firstly adjusted at $\alpha_0 = 4º$. When it was already moving, depending on the phase angle a different geometrical angle of attack was adopted due to the airfoil's pitching motion – $\alpha(t)$ – whose amplitude is 7.46º.

Moreover, the heaving motion induces a modification of the geometrical angle of attack into an effective one. In the middle of the downstroke, $\alpha = -3{,}46º$ has a variation of $\zeta = 11.46º$, obtaining $\alpha_{eff} = 8º$. In the middle of the upstroke, at phase angle 270º, $\alpha = 11{,}46º$, but the variation leads this angle to a 0º effective angle of attack.

Note that the variation on the 0º –top dead center– and 180º phase angle –bottom dead center– is zero, therefore the geometrical and effective angle are equal: 4º.

2.2 Particle Image Velocimetry

Particle Image Velocimetry is a non-intrusive measurement method able to capture the instantaneous flow field. One of its most important advantage is that allows to record images of the whole velocity flow field, compared with other techniques which allow only the measurement at a single point. Its principle is based on the quantification of the displacement of small tracer particles which are carried by the fluid during a short time interval.

These particles have to be small enough to follow the fluid motion without altering it, but big enough so that the camera sensor can detect their scattered light [2]. They are illuminated twice by a thin light sheet usually generated by a double-pulsed laser system (see Fig.2-3). A digital imaging device is in charge of recording the light scattered by the particles on two subsequent frames.

The cameras are directly connected to computer which processes all the data with the adequate software, like Davis from LaVision.

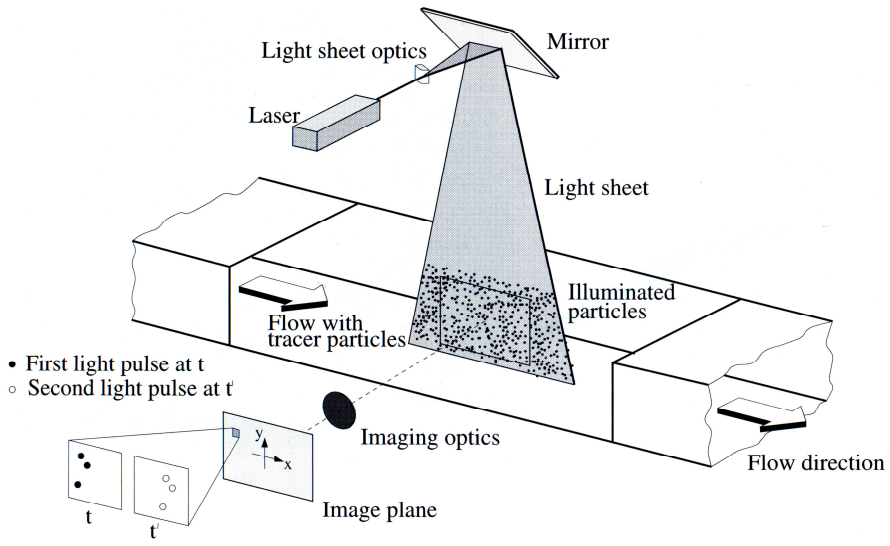

Fig. 2-3 Experimental setup for PIV in a wind tunnel

It is important to take into account that the PIV technique needs optical access for the laser light sheet and also for the cameras in the test section. When doing standard PIV – measurement only of two velocity components- the camera must be aligned normal to the

light sheet plane. That it is not necessary when Stereoscopic PIV is being done –measurement of the three velocity components-.

▪ Equipment

To illuminate the tracer particles a light source is required. An important requirement for this source in PIV is a short duration of illumination dt, to avoid image blurring. The pulse duration has to be able to catch the particles as dots rather than streaks. In addition, it has to have enough intensity so that the scattered light by the seeding particles can be detected by the digital cameras.

Pulsed lasers are the most widely light resources being used in PIV. They consist on two separate lasers firing independently at the required pulse separation. The most common one is the solid-state doubled Nd:YAG laser which emits light with a wavelength of 532mm.

A set of adequate lenses convert the delivered laser beam into a thin light sheet.

For image capturing, the cameras with CCD –Charged Coupled Device- are the most broadly used. CCDs are electronic sensors that convert light into electronic charge.

▪ Seeding

Laskin nozzle (see Fig.2-4 and Fig.2-5) is the most extended seeding supplier in PIV measurements [3]. Normally filled up with oil which offers the advantage of not being toxic, it stays in air at rest for a long time and do not change in size significantly under various conditions.

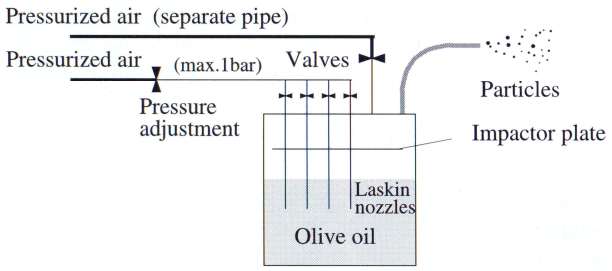

Fig. 2-4 Seeding supplier scheme

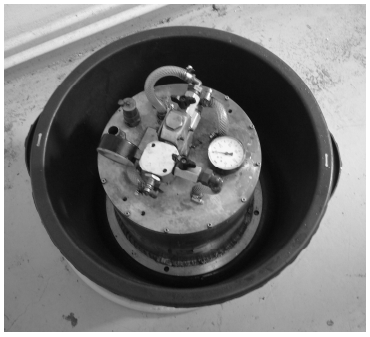

Fig. 2-5 Oil seeding generator

2.2.1 Digital image processing

Once the double-frame recording of the experiment is done, the data stored in computer is ready for being processed. Before starting with the velocity vector computation, it is sometimes necessary to do an image pre-processing. In this case, there are two kinds of initial corrections: image restoration to repair undesirable effects due to imaging –such as perspective distortion- and image improvement to accentuate some image features –such as image contrast modification-.

An optimal image processing implies a homogeneous seeding, uniform illumination and uniform image background during the data acquisition process. Sometimes it is difficult to keep a uniform background due to reflections. However this can also be solved with pre-processing methods.

When the PIV recording is done through the 'double frame / single exposure' technique the evaluation of the images is performed by cross-correlation –or stereo cross-correlation- [4]. Herein, the complete image is subdivided in interrogation windows and each of it will be evaluated separately, obtaining a vector as a result (see Fig.2-6).

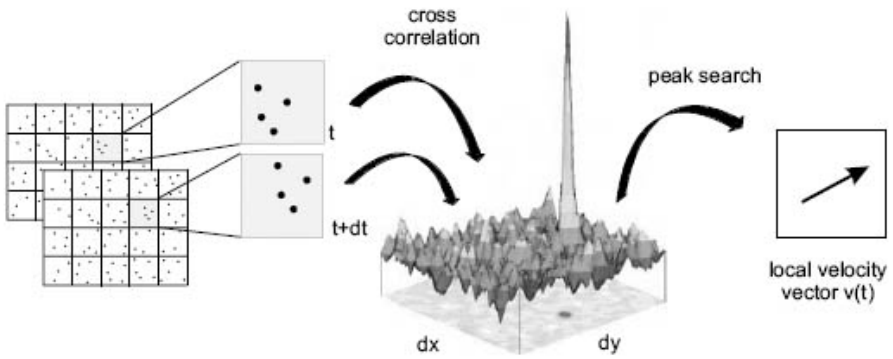

Fig. 2-6 Evaluation of PIV recordings through cross-correlation

Two important requirements to get a higher correlation peak: the displacement of the particle images within the interrogation domain should be almost uniform, and the interrogation domain should contain a considerable number of particle image pairs.

Automatic post-processing data in PIV is really significant. Then, investigations with PIV usually require lots of images which are not possible to evaluate by hand. So, it is useful to do an automatic validation of the data to delete the wrong vectors, replace incorrect information or do the average velocity vector field, for example.

3 EXPERIMENT I

The purpose of this first experiment is to measure the boundary layer, over a flexible and non-flexible SG04 airfoil (see Fig.3-1), and to locate the laminar separation bubble phenomena with the Stereo PIV technique.

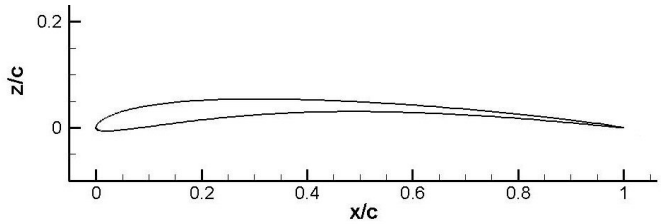

Fig. 3-1 SG04 airfoil, imitating the seagull's one

For this aim the setup was done in a low speed, low noise LNB wind tunnel (see Fig.3-2), which is an Eiffel style construction [5]. The closed test section measures 600x400x1500mm. Its maximum velocity in the test section is of 19m/s and the turbulences are lower than 0.1% at 10m/s.

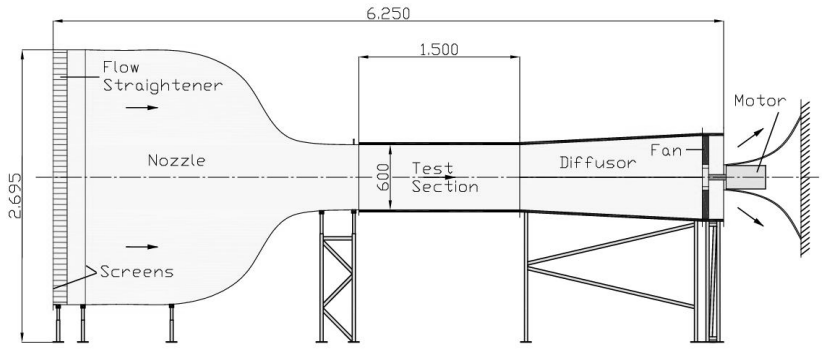

Fig. 3-2 LNB wind tunnel

Around the test section, an installed flapping flight motion apparatus provided the SG04 of a heaving and pitching movement. The heaving amplitude of this device is 10cm.

3.1 Experimental setup

To carry out this experiment a double pulsed Nd:YAG laser was set on the top of the wind tunnel.

Two SensiCams with 180mm objectives were placed on each side of the tunnel test section (see Fig.3-3). These objectives only allow capturing an area of around 2cmx2cm over the airfoil. For this reason, if it was wanted to determine the flow on the whole airfoil surface, multiple measurements needed to be done, displacing by hand both cameras.

A seeding generator provided oil particles to the flow.

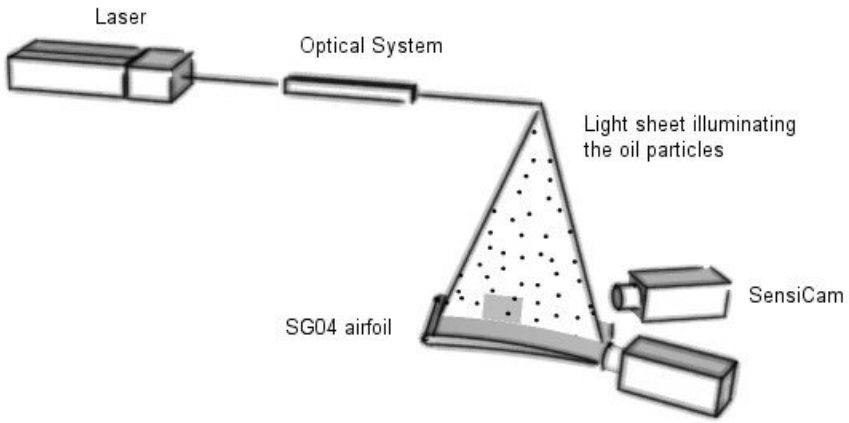

Fig. 3-3 Two cameras Stereo PIV measurement scheme

▪ Laser and optical system

The first important aim in this experiment was to set accurately the light source for illuminating the oil particles in the upper part of the airfoil. To do so, one light sheet was required.

The circular cross-section beam delivered from the laser had to be shaped into a thin light sheet. For this conversion a lenses system assembly in a micro-bank had to be

considered. Also it had to be checked that the laser beam crossed the lenses exactly through the middle.

The collection of used lenses was: a divergent spherical -50mm lens, a convergent spherical +80mm lens and a divergent cylindrical -25mm one. At the end a mirror was placed in order to reflect the new light sheet downwards.

After the setting of the light plane, it was important to ensure that it was in the middle of the wind tunnel and, completely parallel to the flow direction and perpendicular to the floor. Their thickness had to be very small to be able to avoid big reflections, but large enough so that the necessary particles to do Stereo PIV could be seen -about 2mm-.

▪ Cameras setting

By means of a beam structure two SensiCams (see Fig.3-4) with 180mm objectives were installed on each side of the test section, each of them attached to a one-degree-of-freedom-device, parallel to the light sheet.

Fig. 3-4 SensiCam with 180mm Tamron objective

These objectives allow only capturing an area of around 2cmx2cm over the airfoil. Thus, to determine the flow on the whole airfoil surface, multiple measurements have to be done, displacing carefully both cameras by hand. This demands a very accurate setting, otherwise at the end of the recording process –windows sequence along the airfoil- they will not match together.

Once it was ensured both cameras looked at the very same place, it was time to focus with the objectives. To obtain a much clearer image and a better result it is worth to focus using the oil particles and the laser light sheet –like when doing PIV recording-.

▪ Calibration

For this Stereo PIV case, a three-dimensional calibration was done. A really thin calibration grid attached to a rigid plastic surface –to avoid deformation– was used.

This grid was fixed in a gadget which allowed her being moved very accurately on the z-axis.

With the Davis software three positions along the z-coordinate were recorded, each one separated by a distance of 1mm: -1, 0 and 1. The second image -position 0- has to fit exactly with the laser light sheet. Otherwise the error is increased.

3.2 Data recording

This experiment was performed in the LNB wind tunnel at 8m/s, and recorded with DaVis from LaVision. It had two different parts.

First aim was to capture the flow on the upper surface while the airfoil was moving upwards and downwards with the flapping apparatus at a 10.3Hz frequency. This measuring was done with the flexible –0˚, 90˚– and non-flexible airfoil –0˚, 90˚, 180˚–.

Secondly, a stationary recording was done also with the two airfoils with an angle of attack of 0˚, 1.17˚, 4˚ and 8˚.

For each one of the above cases, the flow over the airfoil was captured with twelve small windows of about 2cmx2cm for a better approach to the boundary layer (see Fig.3-5). After each recording of 1000 images, the two cameras on each side were displaced 2cm at the same time with the one-degree-of-freedom-device. As the cameras were looking into the wind tunnel from the trailing edge, the oncoming flow on the leading edge could not be seen. Therefore, both cameras were then installed at the front –looking from the leading edge– to record also this part. With two windows from here was enough.

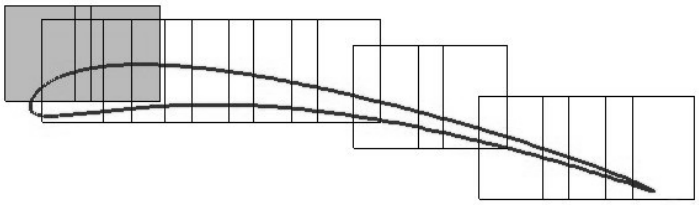

Fig. 3-5 2cmx2cm windows above the airfoil, twelve are needed to cover the whole chord. The two darker windows were recorded by the camera from the front.

In each recording, first a normal photo with a calibrated grid adapted to the airfoil's form was done (see Fig.3-6), to know which part were we looking at. Then the whole room was filled with oil particles, and the 1000 images recording could be started (see Fig.3-7).

The optimal PIV results are when the particle shift is around ten pixels. So, the time interval between the two images had to be adjusted to fulfill this aim.

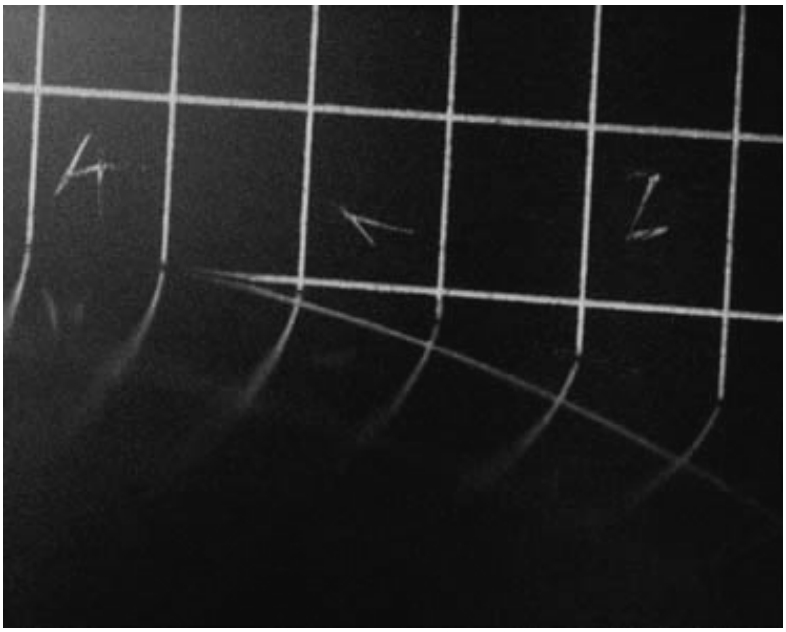

Fig. 3-6 Airfoil with calibration grid

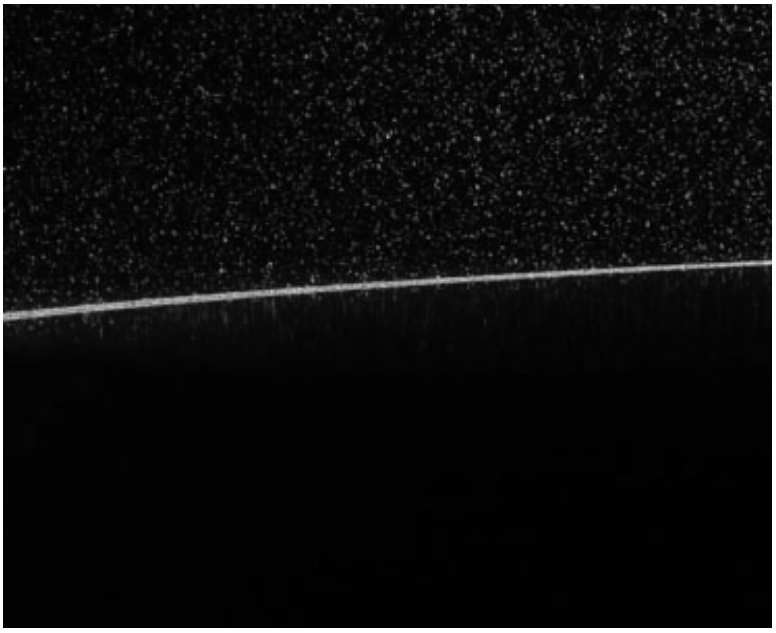

Fig. 3-7 Particle image of non-flexible SG04 at the bottom dead center.

3.3 Data processing

Once all the image sets are recorded, raw data processing with the same software can be done.

However, in the moving airfoil cases pre processing is required: the wing's picture is taken once per flapping cycle at the same desired phase angle, but still the airfoil can have a slightly different position. This can be easily solved with shift and rotation correction.

With the 1000 samples already corrected, the area for velocity distribution computation had to be defined. With a mask only the zone with oil particles had to be selected, otherwise false results could be obtained.

Velocity vectors could be calculated through stereo cross-correlation for each subsequent pair of images. When the images of both cameras were not exactly the same, stereo cross-correlation could not be carried out, so cross-correlation was done.

Multi-pass cross-correlation was executed, starting with 32x32px windows –sometimes with 64x64px when velocity was higher– and decreasing until 12x12px ones. An overlap of 50% and a round weighting function was performed (see Fig.3-8 and Fig.3-9).

After this process, the spurious results were removed with a vector post processing filter. Then, the average velocity and RMS fields could be computed.

All necessary data was sent to TECPLOT, were the twelve data windows from each airfoil upper surface could be merged down in one single picture, to analyze the phenomena along the whole chord, and calculate other variables like turbulent shear stress.

▪ Shear stress calculation

The turbulent shear stress helps to locate the transition from laminar to turbulent flow: $\tau_{xy} = -\rho \cdot \overline{u'v'}$. Negative values indicate the presence of turbulence in the area.

Where the shear stress starts, it is the same point where the laminar separation bubble phenomena finishes [6].

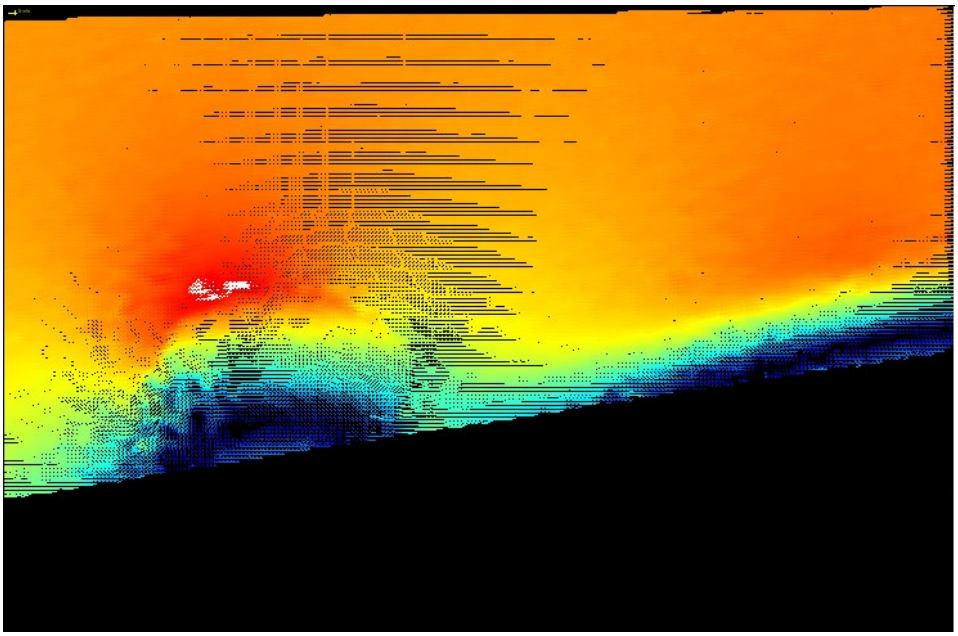

Fig. 3-8 Instantaneous velocity vector field of a 2cmx2cm window from a non-flexible stationary airfoil, $\alpha = 4º$

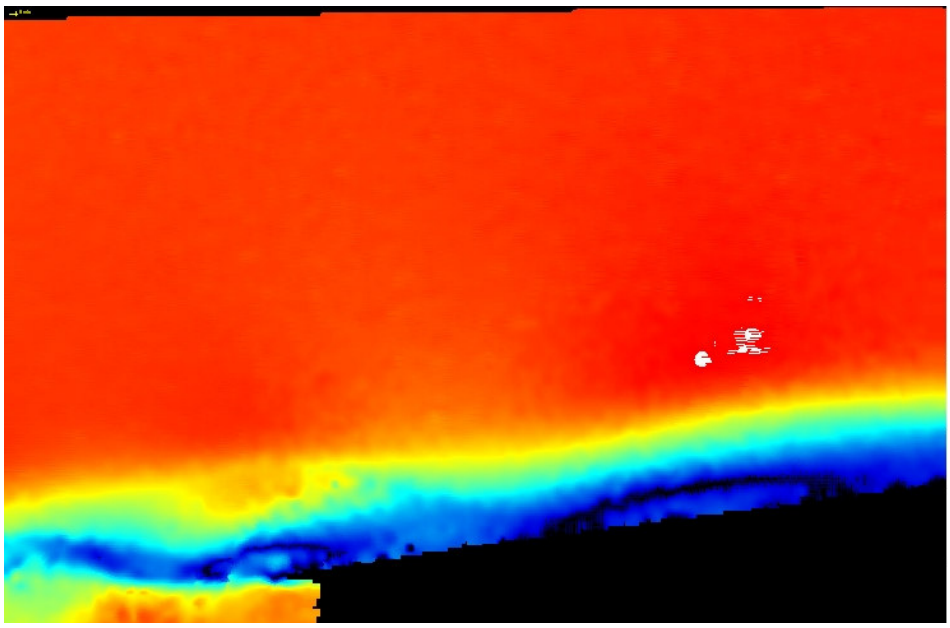

Fig. 3-9 Instantaneous velocity field of the 2cmx2cm window of the trailing edge from a flexible stationary airfoil, $\alpha = 1.17º$

3.4 Results

In this section the turbulent shear stress between some flapping and stationary, and flexible and non-flexible airfoils is depicted. In one case, velocity is also shown.

The results over a flexible and non-flexible airfoil with the same angle of attack, $\alpha = 1.17º$, are presented (see Fig.3-10). Over the non-flexible SG04 the turbulent shear stress has a stronger value. However, over the flexible airfoil a weak transition starts earlier –before the trailing edge– on the 95% of the chord length.

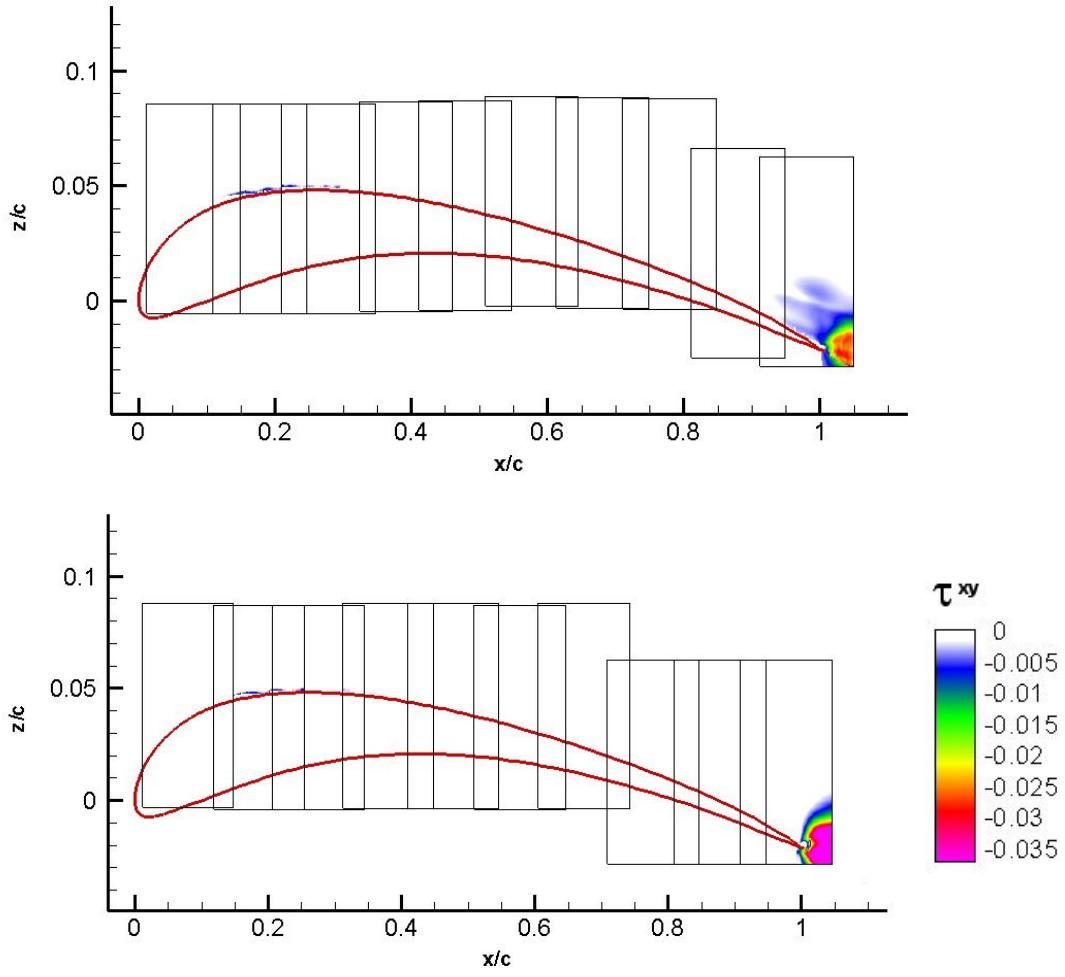

Fig. 3-10 Stationary flexible (top) and non-flexible (bottom) airfoils with $\alpha = 1.17º$

Three different situations with the non-flexible SG04 airfoil are shown: stationary $\alpha = 4º$ case, moving airfoil at 180º phase angle case and moving airfoil at 0º phase angle case. They all have in common that their effective angle of attack is 4º.

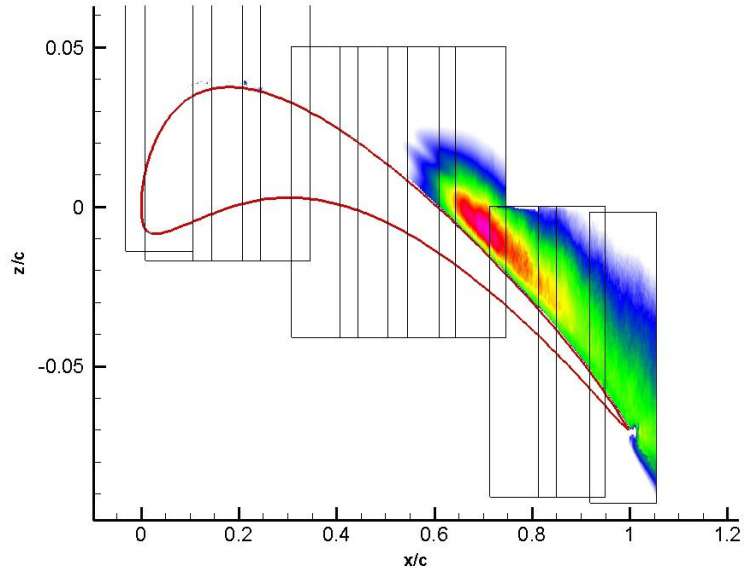

Fig. 3–8 Turbulent shear stress over a non-flexible stationary $\alpha = 4º$ airfoil

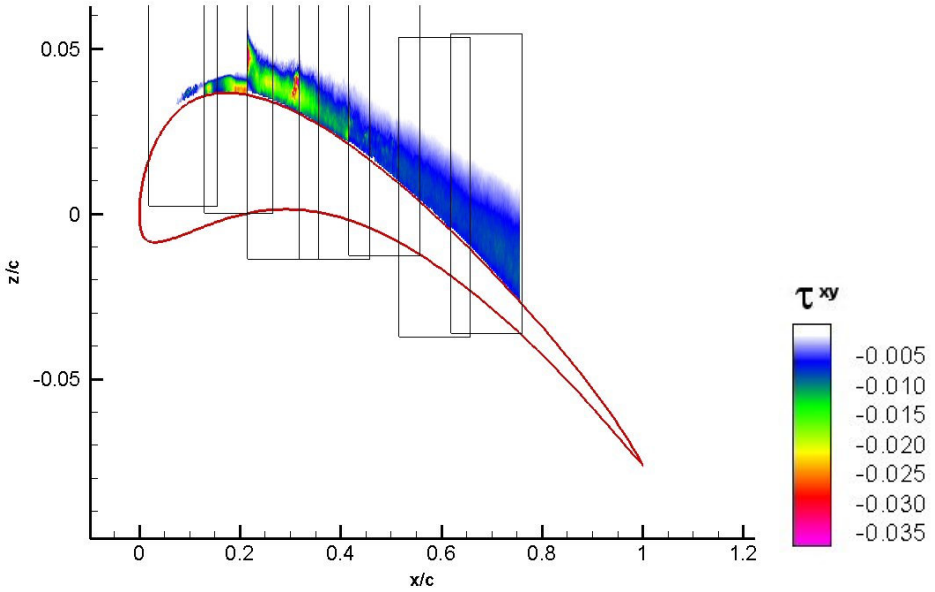

Fig. 3–9 Turbulent shear stress over a non-flexible flapping airfoil, at 180º phase angle **.**

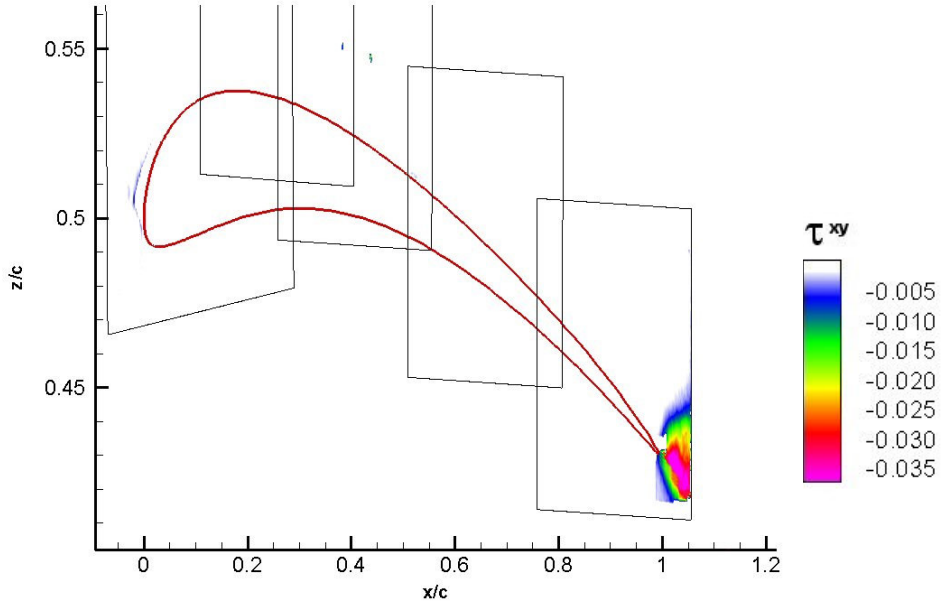

Fig. 3-10 Shear stress over a non-flexible SG04 at 0º phase angle.
Results of Dipl.-Ing. Stephan Bansmer, TU Braunschweig.

Over the stationary non-flexible airfoil with $\alpha = 4^{a}$ the turbulent shear stress starts around the 60% of the chord length and it has its maximum rate in the 70% (see Fig.3-8). On the other hand, over the non-flexible SG04 at 180ª phase angle case, the τ_{xy} is starting closer to the leading edge, at the 10% of the chord length (see Fig.3-9). Here the values of the shear stress are not so agressive like the stationary case.

Lastly, a non-flexible flapping airfoil at the top dead center is depicted (see Fig.3-10). The effective angle herein is the same as the two last cases. Though, the transition from laminar to turbulent flow takes places at the trailing edge.

The representation of the velocity field of the two previous cases is shown in the following charts (see Fig.3-12 and Fig.3-13).

In Fig.3-12 the boundary layer separates from the airfoil surface –60% of the chord length–, at the same place where turbulent shear stress appears in Fig.3-8. In this point is were the laminar separation bubble phenomena appears. The same occurs with the flapping airfoil phase-locked at the bottom dead center.

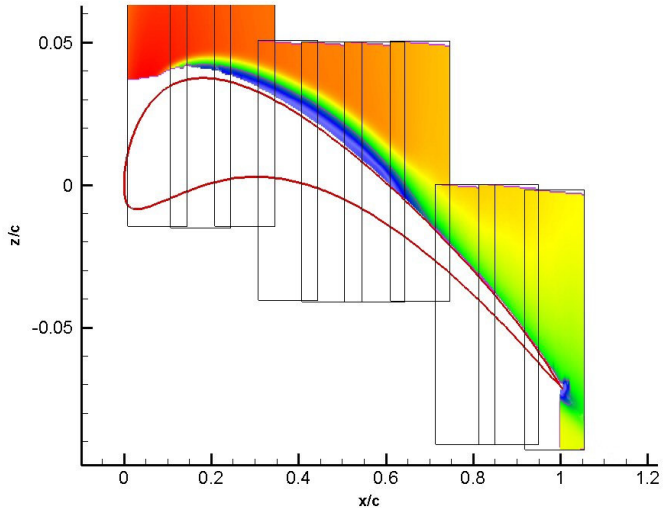

Fig. 3-11 Velocity field of a stationary non-flexible airfoil at $\alpha = 4º$

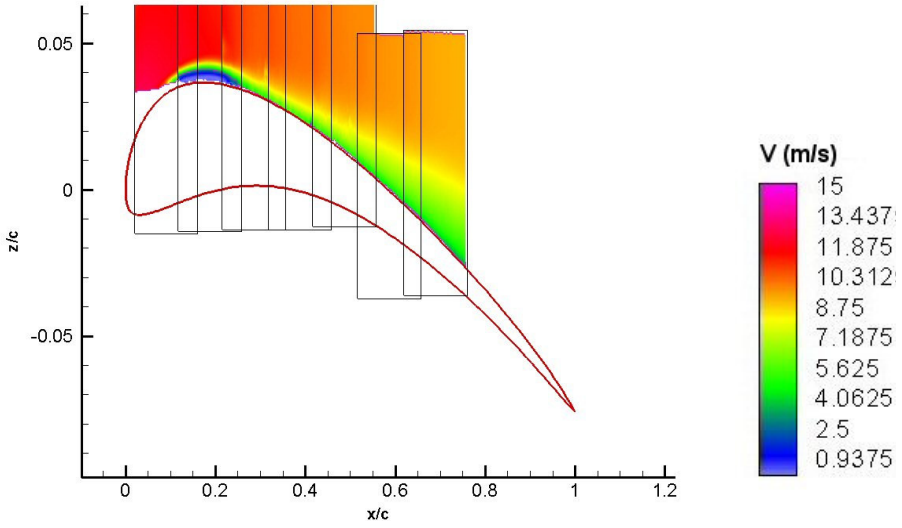

Fig. 3-12 Velocity field of a non-flexible flapping 180º phase angle airfoil

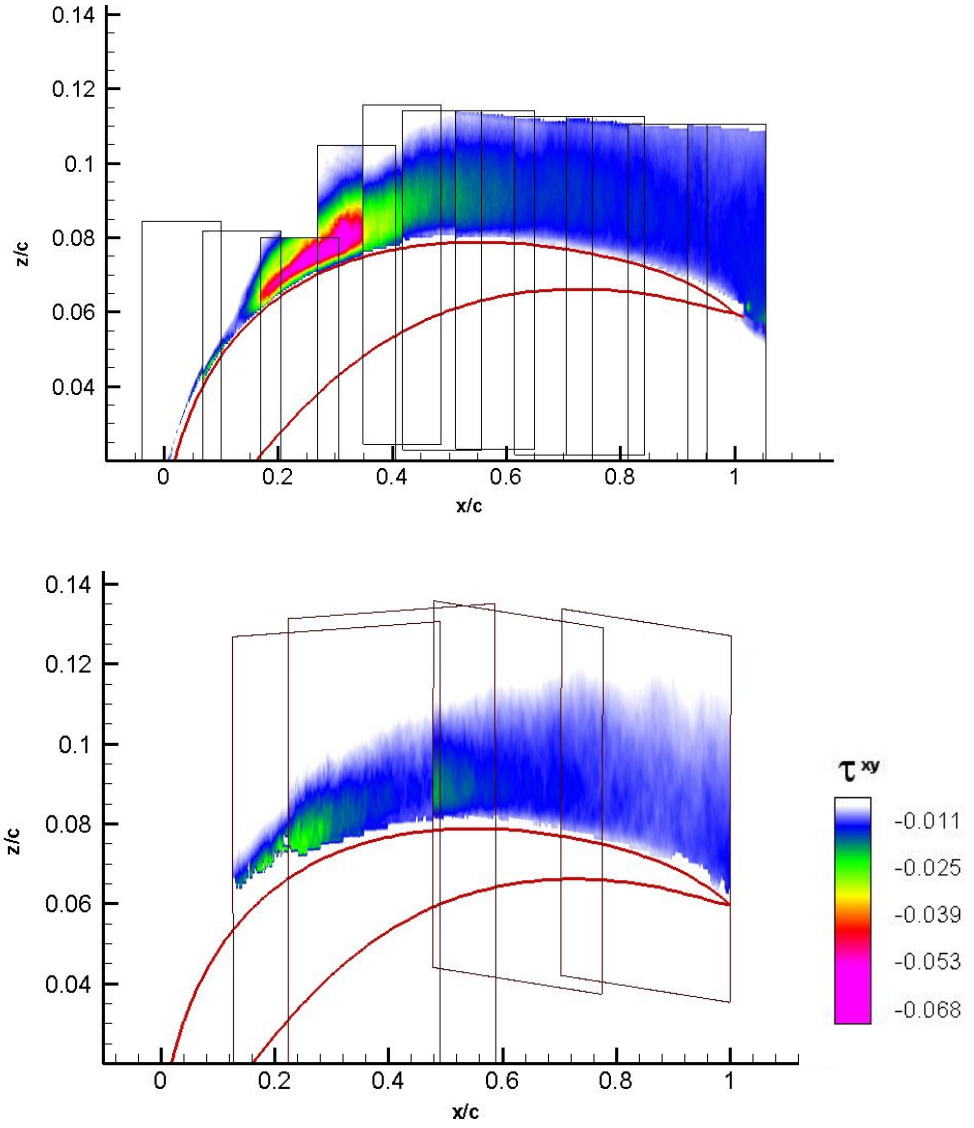

Fig. 3-13 τ_{xy} of a non-flexible airfoil at the middle of the downstroke in both cases. Second chart: results of Dipl.-Ing. Stephan Bansmer, TU Braunschweig.

Both previous plots are result of different experiments, but same conditions: non-flexible airfoil at 90º phase angle (see Fig.3-14). Turbulent shear stress arises in both cases at 15% of the chord length. Nevertheless, its maximum value in the first case is more than twice the shear stress in the second chart.

4 EXPERIMENT II

The goal of this second experiment is to measure the velocity field around one flexible SG04 airfoil through Stereo PIV, in order to find out the pressure distribution.

Unlike the previous case, all the flow above and under the wing has to be recorded at once, within the same window. For this aim, lighting the superior and inferior airfoil surface is needed.

4.1 Experimental setup

To fulfill the purpose of this experiment a pair of double pulsed Nd:YAG lasers are required. As Stereo PIV has to be done at the same time on both surfaces, four cameras are essential: two PCO4000 were in charge to capture the upper particle images and two SensiCams recorded the lower part (see Fig.4-1).

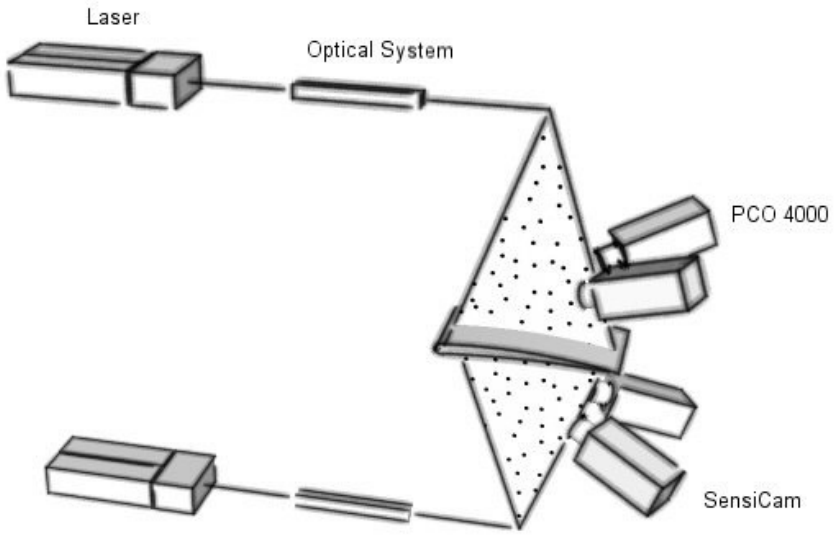

Fig. 4-1 Four cameras Stereo PIV measure scheme

▪ Laser and optical system

To create both faced light sheets, one laser was placed over the wind tunnel and the other one under it, set on a beam structure (see Fig.4-2). So, the first beam reached the airfoil from the top of the test section and the other one, from the bottom.

Fig. 4-2 Doubled-pulsed Nd: YAG laser with optical system, which provides of thin light sheet the inferior airfoil surface.

The lenses used in here for converting the laser beams into thin light sheets are the same as in the previous experiment. The requisites to accomplish by both light planes are also the same: in the middle of the test section, parallel to the flow direction and perpendicular to the floor. But it was even more important to check that both lights lay on the same plane.

▪ Cameras setting

The following step was to fix the four cameras on a beam system, two in each side of the wind tunnel. A couple of PCO4000 cameras faced the over surface of the airfoil, equipped with 105mm objectives. The two SensiCams with 28mm objectives looked toward the bottom part.

The four cameras had to meet at the same area, which in fact is fast the entire airfoil extension. To make easier to define it, the calibration grid was used so that the four cameras were shifted until the view field was the same.

As said before, focus the objective with the oil particles improves the results.

▪ Calibration

This time the three-dimensional calibration was made using a grid glued on a thin glass plate. Once this grid was placed in the test section, the calibration with Davis could be executed.

Ideally the grid should have 0mm thickness. In reality it is not possible, so a so-thin-as-possible grid has to be used. Moreover, the grid is only printed on one side of the calibration panel. So, the cameras recording from the other side had to look through this panel and the resulting images are slightly different. This is caused by the diffraction phenomena in the glass/plastic panel: the way from one camera to the grid is not total straight, although it is from the cameras looking from the other side.

However this small deviation can be later corrected with the so-called “disparity map” when doing the evaluation of the recorded images with the software, by means of cross-correlating the simultaneous particle images recorded from the two cameras.

4.2 Data recording

Alike the previous experiment, this one was performed at 8m/s and a 10.3Hz frequency, three times: first with the two upper cameras, second with the two lower cameras and third, with the four cameras together.

For each case three different measurements with the flexible airfoil were made: in the stationary case, during the middle of the upstroke and during the middle of the downstroke. Each recording took a sample of 1000 images.

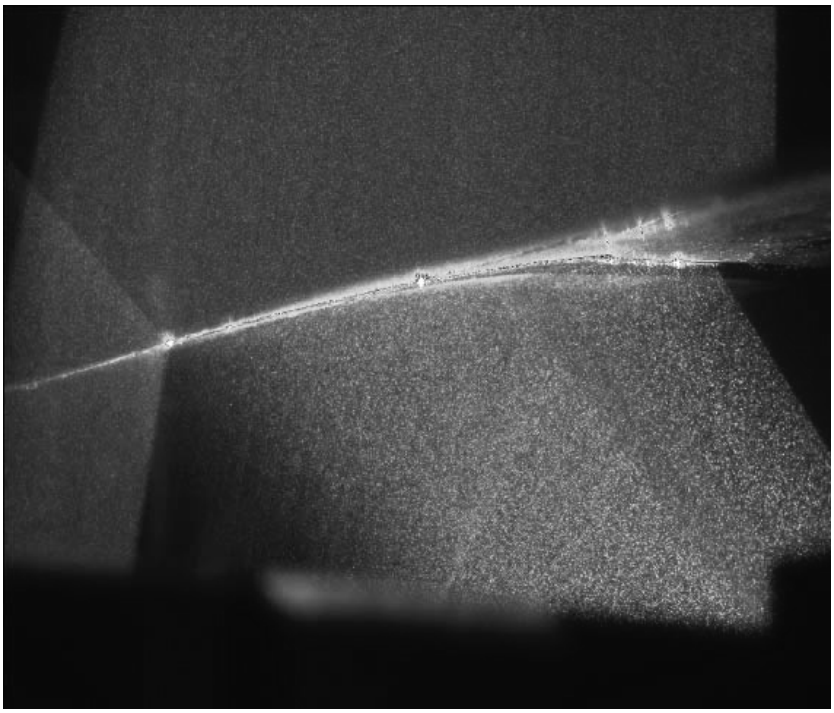

Fig. 4-3 Particle image of SG04 during the upstroke, lighted on both sides

4.3 Data processing

In this case, before starting with pre processing, a self-calibration for disparity map correction was required. This must be done when normal calibration with the grid is not good enough or its thickness, for example, induced to an inexact coordinates system.

In this experiment, a part of having done shift and rotation correction, the strong reflections of both laser sheets had to be removed. Therefore, for each data set an average intensity image was computed, and then subtracted of each single sample. After this process, the particle pictures had a better quality.

Vector field computation of the upper and lower surface had to be done separately: first, an upper mask was drawn and the whole velocity field calculated, and then, the second mask was made.

In Stereo PIV, interrogation windows started from 64x64px and decreased until 16x16px windows.

The next step was vector post processing, as in the first experiment: eliminate wrong vectors and compute de average velocity (see Fig.4-4 and Fig.4-5). Results to be mapped can be already exported to TECPLOT.

With the same software the pressure coefficient will be found out around the SG04 airfoil.

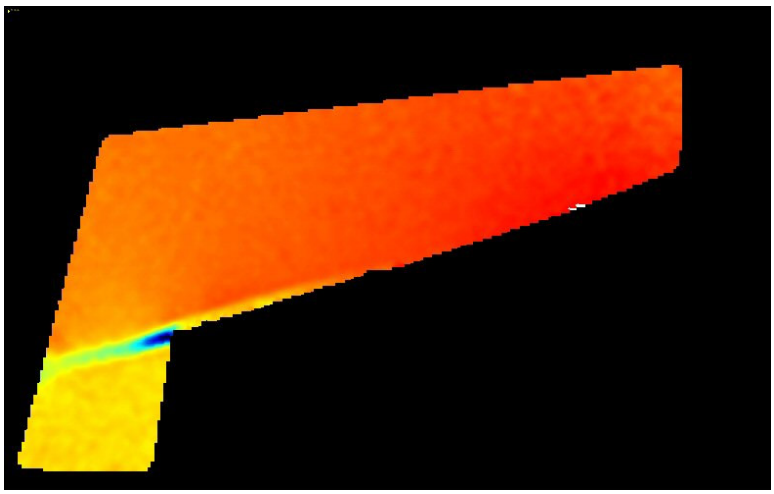

Fig. 4-4 Average velocity field at the middle of the upstroke on the suction side of a flexible SG04 (first mask)

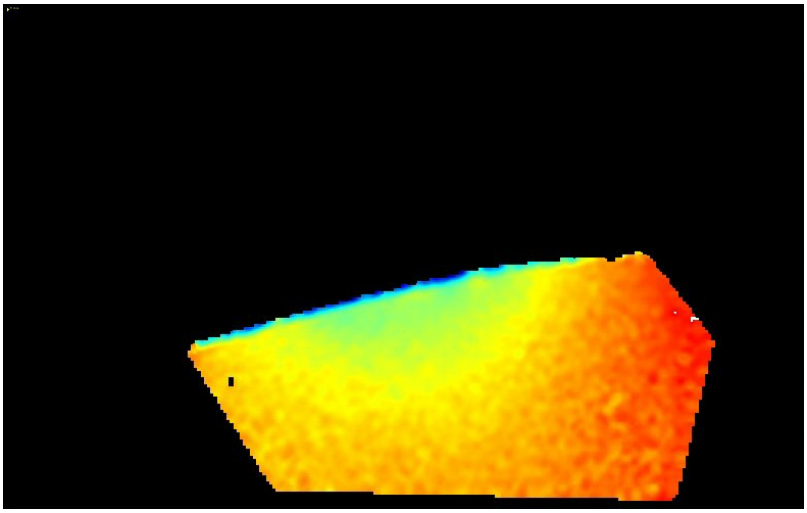

Fig. 4-5 Average velocity field at the middle of the upstroke on the lower side of the flexible SG04 (second mask)

▪ Pressure distribution calculation

To calculate this distribution two main equations are used: the Bernoulli (1) and the pressure coefficient (2) equations.

$$p_\infty + \frac{\rho}{2} u_\infty^2 = p_1 + \frac{\rho}{2} u_1^2 \quad (1)$$

$$Cp = \frac{p_1 - p_\infty}{\rho/2\, u_\infty^2} \quad (2)$$

Where p_∞ and v_∞ refer to unperturbed flow (see Fig.4-7), and data around the airfoil is included in p_1 and v_1. Merging these two equations, the following one is obtained: $Cp = 1 - \frac{u^2}{u_\infty^2}$ and computed with TECPLOT.

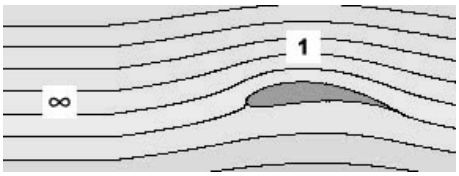

Fig. 4-6 Flow around the airfoil

Although this expression is applied in the experiment, note that it might be only used for steady flows.

4.4 Results

This part includes the pressure distribution around the flapping flexible SG04 airfoil in two cases: middle of the downstroke and middle of the upstroke.

This case recordings were done once with the two upper cameras, once with the two lower cameras and another time with the four cameras together. However, here only the four cameras case is depicted.

In the middle of the downstroke, the airfoil has a -3,46º geometrical angle of attack, but due to heaving motion the effective angle of attack is of 8º (see Fig.4-8). On the suction side the leading edge has the lowest pressure coefficient and this one get higher radially when the chord length increases.

On the lower side pressure is distributed the other way round. When approaching to the leading edge Cp has a higher value which decreases with the chord length advance. Herein, there is no data available near the trailing edge because the laser light sheet could not cope with the whole wing chord.

On the trailing edge the highest pressure is found as a result of the mixing of the to flows.

Moreover, due to laser reflections on the surface, velocity vectors close to the airfoil could not be calculated. So, pressure distribution can not be representated.

The pressure distribution in the middle of the upstroke is depicted (see Fig.4-8). The SG04 has a geometrical angle of attack of 11.46º, but the effective one is 0º.

Unlike the previous case, on the upper section the minimum pressure point is not on the trailing edge, this time it has moved to the 20% of the chord length. On the other side, the maximum pressure is displaced at the 65% of the chord length.

Also in this graphic, the maximum pressure is at the trailing edge.

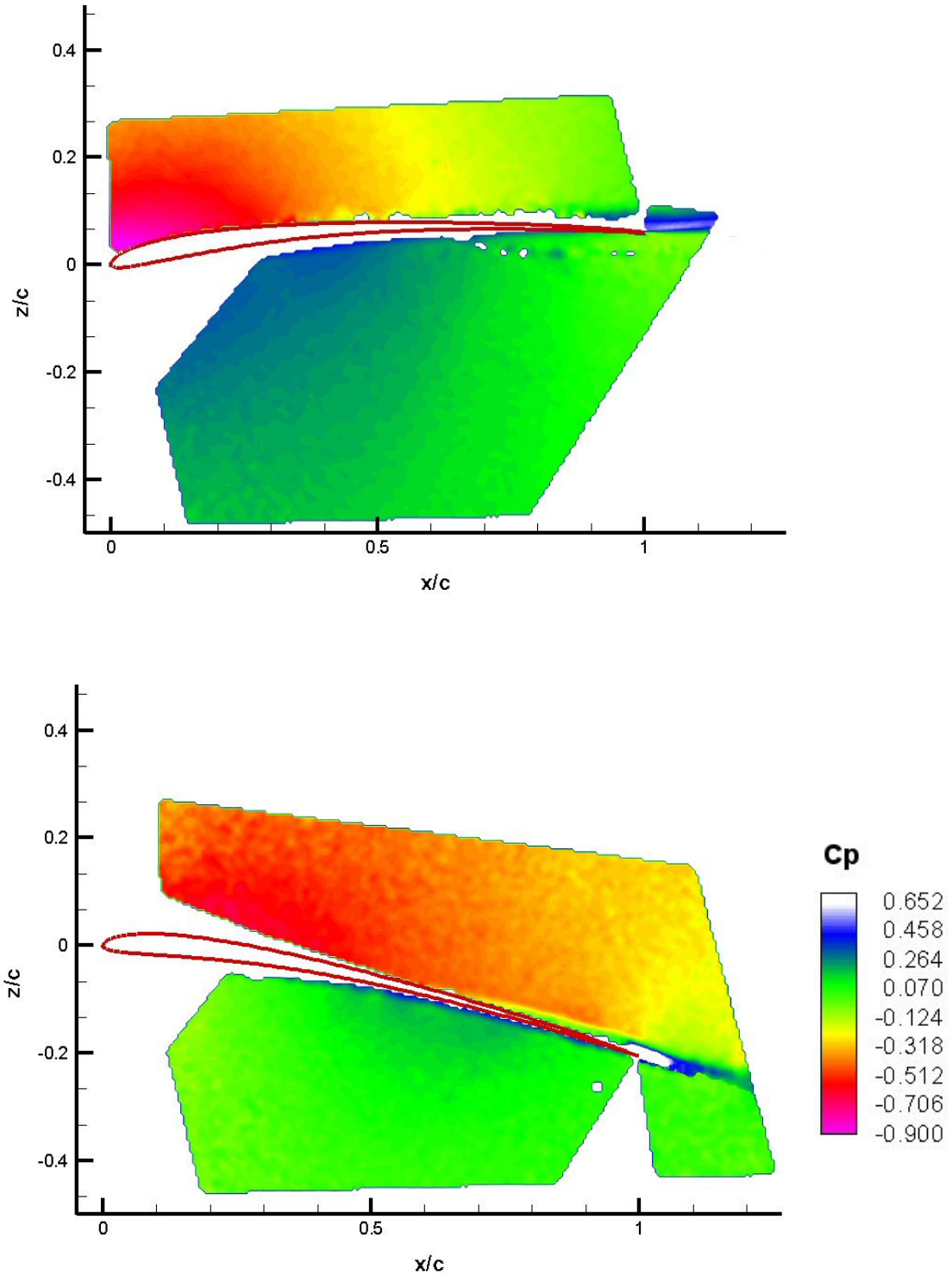

Fig. 4-7 Cp of a non-flexible flapping airfoil at the middle of the downstroke (top) and at the middle of the upstroke (bottom).

5 SUMMARY

Particle Image Velocimetry is a measuring method which requires a lot of time: first, to set up the experiment and then, to do the recording and the data processing.

In the first experiment, quality measurements very close to the airfoil surface could be done. This optimal recording of the boundary layer and the data pre processing in DaVis to enlarge the noise to signal ratio of the samples, facilitated the further detection of the turbulent shear stress.

In the second test was harder to take good pairs of images. Then, the laser reflections were more difficult to control and the area of interest was bigger, including also the lower surface of the wing. For this reason the pressure distribution results in chapter 4.4 have a poor quality when nearing the airfoil. However, the general pressure distribution can be seen.

Highlighting the flapping non-flexible airfoil case, it can be seen from the charts in chapter 3.4 that the turbulent shear stress arises on a different place depending of the phase angle –0 º, 90º and 180º–. At 0º it is at the trailing edge. When the 90º phase angle is performed, the transition from laminar to turbulent flow is at 15% of the chord length, and this transition moves until the 10% of the chord length if the airfoil is on the bottom dead center. Therefore, knowing that in this transition the laminar separation bubble is found, can be assumed that it moves along the airfoil, when it flaps.

6 REFERENCES

[1] Bansmer S, Mazlum E, Radespiel R. *A Comparison of numerical RANS simulations and flow field measurements of an oscillating airfoil for flapping wing propulsion*. ICAS 2008.

[2] Tropea C, Yarin A, Foss J. *Handbook of experimental fluid mechanics*. Springer. Berlin, 2007.

[3] Raffel M, Willert C, Wereley S, Kompenhaus J. *Particle Image Velocimetry. A Practical Guide*. Second edition. Springer. Berlin, 2007.

[4] LaVision. *DaVis Flowmaster Software Manual*. LaVision GmbH. Göttingen, 2005.

[5] http://www.tu-braunschweig.de/ism/

[6] Bansmer S, Scholz U, Windte J, Kähler C, Radespiel R. *Flow Field Measurements on an Oscillating Airfoil for Flapping Wing Propulsion.* AIAA 2008-581.